This is the accepted manuscript made available via CHORUS. The article has been published as:

Geometric effects in the effective-mass theory and topological optical superlattices

Chao-Kai Li, Qian Niu, and Ji Feng

Phys. Rev. A **98**, 041603 — Published 31 October 2018

DOI: 10.1103/PhysRevA.98.041603

Geometric effects in the effective-mass theory and topological optical superlattices

Chao-Kai Li,[1] Qian Niu,[2] and Ji Feng[1,3,4,*]

[1] *International Center for Quantum Materials, School of Physics, Peking University, Beijing 100871, China*
[2] *Department of Physics, The University of Texas, Austin, TX 78712-0264, USA*
[3] *Collaborative Innovation Center of Quantum Matter, Beijing 100871, China*
[4] *CAS Center for Excellence in Topological Quantum Computation, University of Chinese Academy of Sciences, Beijing 100190, China*

(Dated: October 8, 2018)

Cold atoms tailored by an optical lattice have become a fascinating arena for simulating quantum physics. In this area, one of the important and challenging problems is creating effective spin-orbit coupling (SOC), especially for fashioning a cold atomic gas into a topological phase, for which prevailing approaches mainly rely on the Raman coupling between the atomic internal states and a laser field. Herein, a new strategy for realizing effective SOC is proposed by exploiting the geometric effects in the effective-mass theory, without resorting to internal atomic states. It is shown that the geometry of Bloch states can have non-trivial effects on the wave mechanical states under external fields, leading to effective SOC and effective Darwin term, which have been neglected in the standard effective-mass approximation. It is demonstrated that these relativistic-like effects can be employed to introduce effective SOC on a two-dimensional optical superlattice, and induce a non-trivial topological phase.

In recent years, topological insulators, in which spin-orbit coupling (SOC) plays a central role, have become a focal spot in condensed matter physics [1, 2]. Cold atom systems, due to their extreme cleanness and high controllability, are expected as an ideal platform for exploring various phenomena related to topological matter as well as the interplay between topology and interaction. In order to synthesize topological insulator in cold atom systems, and to explore many intriguing effects of SOC itself on cold atoms that have no analogue in solid-state systems, it is important to create artificial SOC in neutral atoms [3–7]. This is not an easy task, although quite a few schemes have been theoretically proposed [8–18]. Based on these schemes, effective SOC has been achieved experimentally in both one-dimensional [19–25] and two-dimensional [26, 27] cold atom systems. These methods mainly rely on the coupling of atom's internal states through an additional Raman laser field. Because different types of atoms have different internal excitation structure, these methods are limited by the availability of suitable internal levels that afford Raman coupling and by the lifetime of the excited states. Another problem is that the spontaneous emission between internal states leads to heating of the quantum gases or atom loss.

In this work, a new approach is proposed for the realization of effective spin-orbit coupling by exploiting the geometric effects in the effective-mass theory. The geometric effect is revealed in relativistic-like terms in a new effective-mass equation derived herein. When applied to a cold atom system on an optical superlattice, this theory leads to effective relativistic effects without utilizing the internal structure of atoms, because SOC effect emerges from the geometry of Bloch bands of the host lattice. Consequently, this approach is expected to be versatile for various types of atoms, and free of heating and atom loss due to spontaneous emission. A model 2D optical superlattice is devised to demonstrate the effective SOC effect, which is shown to indeed lead to a topologically non-trivial phase. This approach can be naturally applied to 3D cases.

The effective-mass theory [28–32], initially formulated for an elementary understanding of shallow impurity states in semiconductors, has played a vital role in semiconductor physics. It also has found wide applications in the quantum physics associated with general imperfections of a lattice such as intercalation, quantum dot, and boundaries , and with motion of electrons in a crystal under external fields [33–40]. However, the geometric effects of Bloch electrons in association with Berry curvature and quantum metric, which have drawn a great deal of attention in decades, is conspicuously absent in the traditional effective-mass equation. Consequently, we start by extending the effective-mass approximation to higher order in order to capture the geometric effects arising from Bloch bands. It is shown that the geometric effects are embodied in Berry curvature and quantum metric tensor, which lead to unusual corrections to the traditional effective-mass approximation, bearing remarkable resemblance to the SOC and Darwin term in the non-relativistic approximation of the Dirac equation [41]. Though the effective-mass equation has traditionally been developed in an electronic structure context, as our cold atom application demonstrates, the higher-order effective-mass equation can be profitably employed to understand and tailor wave mechanical states associated an imperfection on a host lattice, including crystals, optical lattices and artificial superstructures.

* jfeng11@pku.edu.cn

In deriving the standard effective-mass equation, a key quantity is the inner product of the cell-periodic parts of Bloch wavefunctions at different $\boldsymbol{k}$-points, $\langle u_{n\boldsymbol{k}}|u_{n'\boldsymbol{k}'}\rangle$. This overlap reflects the metric change of the Hilbert spaces of distinct $\boldsymbol{k}$-points when the Brillouin zone is viewed as a manifold, and is associated with such geometric quantities as Berry curvature and quantum metric [42–45]. Nonetheless, this important geometric quantity is taken as $\delta_{nn'}$ in the traditional effective-mass approximation [32]; that is, at this level of approximation a trivial geometry is always adopted, which can otherwise have highly non-trivial manifestation. For example, the geometric effect has been suggested to play an important role in the excitonic states in 2D semiconductors [46, 47].

We begin by formulating the impurity problem. For a perfect lattice with Hamiltonian H_0 respecting discrete translational symmetry, its eigenstates are the Bloch wavefunctions $|\psi_{n\boldsymbol{k}}\rangle$, with corresponding eigenenergies $\varepsilon_n(\boldsymbol{k})$, n being the energy band index and $\hbar\boldsymbol{k}$ the crystal momentum. When an impurity is placed in a perfect host lattice, the stationary Schrödinger equation is

$$(H_0 + U)\,|\Psi\rangle = E|\Psi\rangle, \tag{1}$$

where the impurity potential U breaks the discrete translational symmetry of the host lattice. The eigenstate $|\Psi\rangle$ can be expanded as

$$|\Psi\rangle = \sum_n \int_{\mathrm{BZ}} [\mathrm{d}\boldsymbol{k}] F_{n\boldsymbol{k}} |\psi_{n\boldsymbol{k}}\rangle, \tag{2}$$

in which $F_{n\boldsymbol{k}}$ is the expansion coefficient, and we use the notation $[\mathrm{d}\boldsymbol{k}] \to V_c \mathrm{d}^d\boldsymbol{k}/(2\pi)^d$ with V_c being the volume of a primitive cell and d the dimensionality. The expansion (2) leads to a set of linear equations of $F_{n\boldsymbol{k}}$,

$$\varepsilon_n(\boldsymbol{k}) F_{n\boldsymbol{k}} + \sum_{n'} \int_{\mathrm{BZ}} [\mathrm{d}\boldsymbol{k}]\, \langle \psi_{n\boldsymbol{k}}\,|U|\,\psi_{n'\boldsymbol{k}'}\rangle\, F_{n'\boldsymbol{k}'} = E F_{n\boldsymbol{k}}. \tag{3}$$

Up to this point, the formulation is exact given the Schrödinger equation (1). Several standard approximations are introduced in the traditional effective-mass approximation [29, 32]. The impurity potential $U(\boldsymbol{r})$ is assumed to be slowly varying in space, and correspondingly, $F_{n\boldsymbol{k}}$ concentrated near an energy band extremum (or a valley) at $\boldsymbol{k}_0$. It follows that the Umklapp scattering can be neglected. With these assumptions, we have

$$\langle \psi_{n\boldsymbol{k}}\,|U|\,\psi_{n'\boldsymbol{k}'}\rangle \approx \frac{(2\pi)^{d/2}}{V_c} U\left(\boldsymbol{k}-\boldsymbol{k}'\right) \langle u_{n\boldsymbol{k}}|u_{n'\boldsymbol{k}'}\rangle_{\mathrm{cell}}\,, \tag{4}$$

where $|u_{n\boldsymbol{k}}\rangle$ is the cell-periodic part of $|\psi_{n\boldsymbol{k}}\rangle$. The subscript "cell" emphasizes that the integral is to be taken over a primitive cell.

Consequently, only the matrix elements $\langle\psi_{n\boldsymbol{k}}|U|\psi_{n'\boldsymbol{k}'}\rangle$ for $\boldsymbol{k} \approx \boldsymbol{k}' \approx \boldsymbol{k}_0$ make a significant contribution in Eq. (3). To the lowest-order, $\langle u_{n\boldsymbol{k}}|u_{n'\boldsymbol{k}'}\rangle \approx \langle u_{n\boldsymbol{k}_0}|u_{n'\boldsymbol{k}_0}\rangle = \delta_{nn'}$ in Eq. (4), as has been adopted in the traditional effective-mass approximation [29, 32]. However, since the quantity $\langle u_{n\boldsymbol{k}}|u_{n'\boldsymbol{k}'}\rangle$ contains the geometric relation between $\boldsymbol{k}$ and $\boldsymbol{k}'$, this approximation amounts to endowing the Brillouin zone, here viewed as a manifold, with a completely trivial geometry.

Now we expand $|u_{n\boldsymbol{k}}\rangle$ to the second order in $\delta\boldsymbol{k} = \boldsymbol{k} - \boldsymbol{k}_0$. It is crucial to keep the expansion up to second order to retain the geometric effects. As detailed in the Supplemental Material (SM) [49], with a suitable gauge choice in one-band scenario, a new effective-mass equation can be obtained,

$$\begin{aligned}\Big[&\varepsilon_n\left(-\mathrm{i}\nabla\right)_{\boldsymbol{k}_0} + U\left(\boldsymbol{r}\right) - \frac{1}{2}\boldsymbol{\Omega}_n\left(\boldsymbol{k}_0\right)\cdot\nabla U\times\left(-\mathrm{i}\nabla\right)\\ &+\frac{1}{2}g_{n,\alpha\beta}\left(\boldsymbol{k}_0\right)\left(\partial^\alpha\partial^\beta U\left(\boldsymbol{r}\right)\right)\Big] F_n\left(\boldsymbol{r}\right) = E F_n\left(\boldsymbol{r}\right),\end{aligned} \tag{5}$$

in which

$$\boldsymbol{\Omega}_n\left(\boldsymbol{k}_0\right) = \mathrm{i}\left\langle\nabla_{\boldsymbol{k}} u_n\right|\times\left|\nabla_{\boldsymbol{k}} u_n\right\rangle_{\boldsymbol{k}_0} \tag{6}$$

is the Berry curvature of the Bloch band [45, 48], and

$$g_{n,\alpha\beta}\left(\boldsymbol{k}_0\right) = \frac{1}{2}\left(\left\langle\partial_{k_\alpha} u_n\right|Q\left|\partial_{k_\beta} u_n\right\rangle + \alpha\leftrightarrow\beta\right)_{\boldsymbol{k}_0} \tag{7}$$

is the quantum metric [43], $Q = 1 - |u_n\rangle\langle u_n|$ is a projection operator. These quantities reflect the geometric effects of Bloch bands and lead to two additional terms to the traditional effective-mass equation, with which the new effective-mass equation has a striking resemblance to the non-relativistic approximation of the Dirac equation [41]. Remarkably, these relativistic-like terms correspond respectively to the spin-orbit coupling and Darwin term. The former can be procured heuristically by re-quantization of effective semiclassical dynamics, but the latter cannot [50]. The present approach has consistently stayed quantum mechanical and is systematic and therefore extensible. And the effective Hamiltonian here involves only gauge-invariant geometric quantities, i.e. the Berry curvature and quantum metric.

The physical meaning of the effective spin-orbit coupling (ESOC) in the new effective-mass equation can be made clearer in a multi-valley scenario. Because the impurity potential is assumed to be slowly varying, the inter-valley coupling—which involves large crystal momentum transfer—can be neglected in the lowest order approximation. Hence, each valley has an independent effective-mass equation (5), which differs from each other by effective mass, Berry curvature, and quantum metric at the valleys. Intriguingly, in the ESOC term the role of "spin" is now played by valleys, and the strength of the "spin"-orbit coupling is proportional to the magnitude of Berry curvature. The appearance of a quantum metric in the new effective-mass equation reflects in part the anisotropy of the host lattice.

Having the new effective-mass equation, we now demonstrate that the ESOC can be exploited to create a 2D topological optical superlattice. The host lattice is taken to be a 2D honeycomb lattice with staggered A-B sublattice potential created by the interference of

six co-planar laser beams, as shown by the six pink arrows in Fig. 1. A horizontal trapping potential is used to confined the atoms to a 2D plane. These six laser beams can be divided into two groups. Each group consists of three laser beams with the same frequency and with 120° angle with each other, generating a triangular lattice by interference. These six laser beams can be generated by three laser sources by the use of acousto-optic modulators, which detune the frequencies between the two groups of laser beams, so as to avoid interference between the two groups, and to control the relative strength of V_A and V_B. Together, the six laser fields generate a host lattice potential

$$V(x,y) = -2V_A\left\{\cos\left[2\pi\left(\frac{x}{a}-\frac{1}{\sqrt{3}}\frac{y}{a}-\frac{1}{3}\right)\right]+\cos\left[2\pi\left(\frac{x}{a}+\frac{1}{\sqrt{3}}\frac{y}{a}+\frac{1}{3}\right)\right]+\cos\left[2\pi\left(\frac{2}{\sqrt{3}}\frac{y}{a}-\frac{1}{3}\right)\right]\right\}$$
$$-2V_B\left\{\cos\left[2\pi\left(\frac{x}{a}-\frac{1}{\sqrt{3}}\frac{y}{a}+\frac{1}{3}\right)\right]+\cos\left[2\pi\left(\frac{x}{a}+\frac{1}{\sqrt{3}}\frac{y}{a}-\frac{1}{3}\right)\right]+\cos\left[2\pi\left(\frac{2}{\sqrt{3}}\frac{y}{a}+\frac{1}{3}\right)\right]\right\}. \quad (8)$$

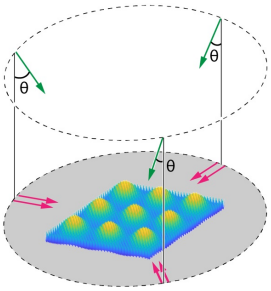

Fig. 1. A proposed experimental setup for the generation of potential $V(\boldsymbol{r})+U(\boldsymbol{r})$ by optical lattice. The colored arrows indicate nine laser beams, which can be obtained by three laser sources. Six of them (pink) lie in the same plane, generating the "host lattice". And the other three lasers (green) point obliquely from out of the plane, generating the "impurity" superlattice. A horizontal trapping potential is used to made the optical lattice two-dimensional.

The two lines of Eq. (8) are generated by the two groups of laser beams, respectively. The parameter a is the lattice constant of this host lattice. Note that if $V_A = V_B$, the six cosines in $V(x,y)$ can be combined into three cosines by sum-to-product identity, and hence three laser beams are enough to generate a honeycomb lattice with inversion symmetry [51]. The difference of V_A and V_B breaks inversion symmetry, and results in direct band gaps at the hexagonal Brillouin zone corners K and K', where the magnitudes of Berry curvature are large [49]. For what follows, we will focus on the conduction band edges at K and K', which are referred to as valleys.

We begin by applying Eq. (5) to analyze the energy levels in the single "impurity" limit, for the two valleys $\boldsymbol{k}_0 = K, K'$. Consider that a large-scale trapping potential $U(\boldsymbol{r})$ is imposed on the host lattice playing the role of an "impurity" potential. Assuming that the trapping potential $U(\boldsymbol{r})$ in Eq. (5) has 2D rotational symmetry, the solutions can be classified by their angular momenta $L_z = l\hbar$, where l is the azimuthal quantum number. For the 2D honeycomb host lattice, the Berry curvature $\boldsymbol{\Omega}$ has the same magnitude and opposite signs at K and K' [49], while the quantum metric g is the same for both valleys. Hence, The ESOC leads to splitting of the otherwise degenerate states with $L_z = \pm l\hbar$, $l \neq 0$. The lowest energy states are two "1s" states originating from the two valleys with vanishing angular momenta. Neither the ESOC nor the effective Darwin term can lift the degeneracy of the two 1s states. In the absence of intervalley scattering, the two 1s states of K and K' valleys are degenerate, and we can treat them as the two spin projections, $|\uparrow\rangle$ and $|\downarrow\rangle$, of a "pseudospin"-1/2.

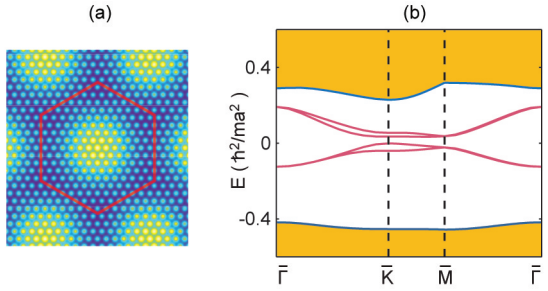

Fig. 2. (a) Schematic of the optical superlattice with potential $V(x,y)+U(x,y)$. A supercell is indicated by the red hexagon. The small dark blue points are the positions of the valleys of the host lattice potential $V(x,y)$, and the small yellow points are the positions of the peaks of $V(x,y)$. So are the large dark blue and yellow areas to the large-scale potential $U(x,y)$. (b) Four minibands (red) are formed in the band gap of the host lattice. The orange regions correspond to the areas occupied bulk bands of the host lattice.

Then we analyze the case when a large-scale 2D honeycomb superlattice, which can be viewed as a periodic array of the above mentioned trapping potentials, is imposed on top of the host lattice. The total large-scale potential $U(\boldsymbol{r})$ (Fig. 2(a)) is no longer fully rotational symmetric, but reduced to the symmetry of a honeycomb superlattice. Because of the hoppings among the

trapping sites, the "impurity levels" become dispersive minibands. With the two 1s states $|\uparrow\rangle$ and $|\downarrow\rangle$ on each trapping site as basis, a tight-binding (TB) Hamiltonian for the large-scale honeycomb superlattice can be built,

$$H = \Delta \sum_{i\mu} \alpha_i c_{i\mu}^{\dagger} c_{i\mu} - t \sum_{\langle ij\rangle\mu} c_{i\mu}^{\dagger} c_{j\mu} + \frac{\mathrm{i}}{3\sqrt{3}} \sum_{\langle\langle ij\rangle\rangle\mu\mu'} (\lambda + \alpha_i \xi)\, \nu_{ij} c_{i\mu}^{\dagger} \left(s_z\right)_{\mu\mu'} c_{j\mu'}, \quad (9)$$

in which $c_{i\mu}^{\dagger}$ creates a particle with pseudospin μ on trapping site i, and $\alpha_i = +1/-1$ for trapping site i lies on the A/B sublattice. 2Δ is the on-site energy difference of the two sublattice originating from the inversion symmetry breaking of the host lattice. The hopping matrix element of the nearest neighbors $\langle ij\rangle$ is denoted as t, and $(\lambda \pm \xi)$ corresponds to the matrix elements of the ESOC between next nearest neighbors $\langle\langle ij\rangle\rangle$ on the A sublattice $(+)$ or B sublattice $(-)$, with the difference 2ξ originating from the inversion symmetry breaking. $\nu_{ij} = +1$ if the direction of $j \to i$ is counterclockwise inside a hexagon of the honeycomb superlattice and -1 if clockwise, and s_z is the z Pauli matrix for $\uparrow$ and $\downarrow$. The Hamiltonian (9) is a generalization of the Kane-Mele quantum spin Hall model [52] to the case of inversion symmetry breaking. The Hamiltonian becomes decoupled in the $\bar{\boldsymbol{k}}$ space of the superlattice, $H = \sum_{\bar{\boldsymbol{k}}} d^{\dagger}(\bar{\boldsymbol{k}}) h\left(\bar{\boldsymbol{k}}\right) d(\bar{\boldsymbol{k}})$, where $d(\bar{\boldsymbol{k}}) = [c_{A\bar{\boldsymbol{k}}\uparrow}, c_{A\bar{\boldsymbol{k}}\downarrow}, c_{B\bar{\boldsymbol{k}}\uparrow}, c_{B\bar{\boldsymbol{k}}\downarrow}]^T$. We use an overbar in $\bar{\boldsymbol{k}}$ to indicate that the wavevector is associated with the superlattice. At the superlattice Brillouin zone corners $\bar{\boldsymbol{k}} = \tau_z\left(\frac{4\pi}{3\bar{a}}, 0\right)$, with $\bar{a}$ the superlattice constant and $\tau_z = \pm 1$,

$$h\left(\bar{\boldsymbol{k}}\right) = \Delta\sigma_z + \lambda\sigma_z\tau_z s_z + \xi\tau_z s_z, \quad (10)$$

in which $\sigma_z = +1$ for A sublattice or -1 and B sublattice. The pseudospin is a good quantum number because $[s_z, H] = 0$. By analogy to the spin Chern number characterizing a quantum spin Hall system [52], a pseudospin Chern number can be defined for the optical superlattice as

$$C_s = \frac{1}{2}(C_{\uparrow} - C_{\downarrow}), \quad (11)$$

in which $C_{\uparrow}$ and $C_{\downarrow}$ are the Chern number of the $\uparrow$ and $\downarrow$ pseudospin branches of the eigenstates, respectively. It is evident from Eq. (10) that the band gaps close at $\bar{K}$ or $\bar{K}'$ of the superlattice Brillouin zone when $|\Delta| = |\lambda|$. For $|\Delta| > |\lambda|$, the pseudospin Chern number is 0, and for $|\lambda| > |\Delta|$ the pseudospin Chern number is ± 1. This means that the presence of the ESOC term in the effective-mass equation (5) is able to drive a topological phase transition of the optical superlattice.

A concrete example of the ESOC-induced topological phase is now provided by numerically solving the above-mentioned superlattice, whose effective-mass theory can be furnished by Eq. (9). The large-scale potential $U(x, y)$ which plays the role of "impurity" potential in the higher-order effective-mass equation (5) is chosen as

$$U(x,y) = 2V_I \left\{ \cos\left[2\pi\left(\frac{x}{A} - \frac{1}{\sqrt{3}}\frac{y}{A}\right)\right] + \cos\left[2\pi\left(\frac{x}{A} + \frac{1}{\sqrt{3}}\frac{y}{A}\right)\right] + \cos\left(\frac{4\pi}{\sqrt{3}}\frac{y}{A}\right)\right\}. \quad (12)$$

This is a honeycomb lattice potential with lattice constant A. Another three laser beams can be introduced to create the large-scale potential (12), as schematically shown by the three green arrows in Fig. 1. They are coming in with angles of incidence θ with respect to the plane of the host lattice. These three laser beams can also be shunted from the three laser sources which generate the host lattice, using acousto-optic modulators and mirrors. Then the relation between the lattice constants A and a is

$$A = a/\sin\theta. \quad (13)$$

In numerical calculations, we use a as length unit, bare mass m of the atom as mass unit, and $\hbar^2/ma^2$ as energy unit, i.e. we set $\hbar = m = a = 1$. Other parameters are chosen as $V_A = 20.0$, $V_B = 20.2$, $V_I = 0.25$, and $A = 12$. The lattice constant $A = 12$ can be realized by choosing the incident angle $\theta = 4.78°$. The superlattice is schematically shown in Fig. 2(a). The Hamiltonian is expanded in a plane wave basis set. The cutoff of the wave vectors is $38\left|\bar{\boldsymbol{b}}_1\right|$ and $38\left|\bar{\boldsymbol{b}}_2\right|$ for the two dimensions, respectively, with $\bar{\boldsymbol{b}}_1$and $\bar{\boldsymbol{b}}_2$ denoting the primitive vectors of the reciprocal lattice of the superlattice.

As expected, four minibands are found in the band gap of the host lattice as shown in Fig. 2(b), originating from the two 1s states of the A and B sublattice: $|A\uparrow\rangle$, $|A\downarrow\rangle$, $|B\uparrow\rangle$ and $|B\downarrow\rangle$. To determine the topological nature of the minibands, let's first investigate the components of the four states at the $\bar{K}$ point of the superlattice Brillouin zone, which reflects the relative magnitudes of $|\Delta|$ and $|\lambda|$ in Eq. (10). The spatial distributions of the particle densities $|\Psi_{\bar{n}\bar{K}}(\boldsymbol{r})|^2$ of the four miniband states $\bar{n} = 1$ to 4 are calculated and shown in Fig. 3(a)-(d). It can be seen that the particle density is localized near the trapping sites of $U(\boldsymbol{r})$, confirming that the minibands are indeed derived from bound states of the trapping sites. The distributions of the projection squared of the miniband states at $\bar{K}$ onto the Bloch states of the host lattice $|F_{\bar{n}\boldsymbol{k}}|^2 = |\langle\psi_{c\boldsymbol{k}}|\Psi_{\bar{n}\bar{K}}\rangle|^2$, $\bar{n} = 1$ to 4 are shown in Fig. 3(e)-(h). We have checked that these four states are constructed almost entirely from the Bloch states $|\psi_{c\boldsymbol{k}}\rangle$ of the

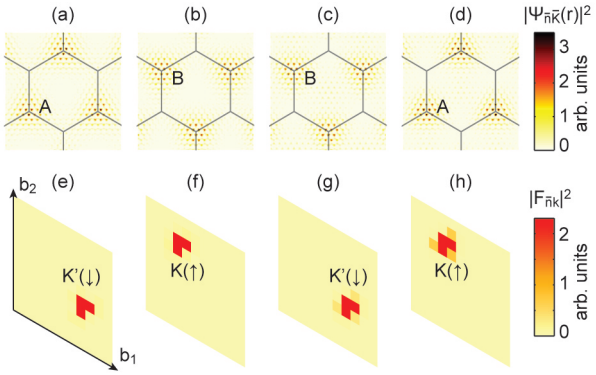

Fig. 3. (a)-(d): Spatial distributions of the particle densities $|\Psi_{\bar{n}\bar{K}}(\boldsymbol{r})|^2$ of the four miniband states at $\bar{K}$ point of the superlattice Brillouin zone, in ascending order of energy. The black lines indicate the honeycomb superlattice. (e)-(h): Distributions of $|F_{\bar{n}\boldsymbol{k}}|^2 = |\langle\psi_{c\boldsymbol{k}}|\Psi_{\bar{n}\bar{K}}\rangle|^2$ of the four miniband states at $\bar{K}$ point, in ascending order of energy. The parallelograms are primitive cells of the reciprocal of the host lattice.

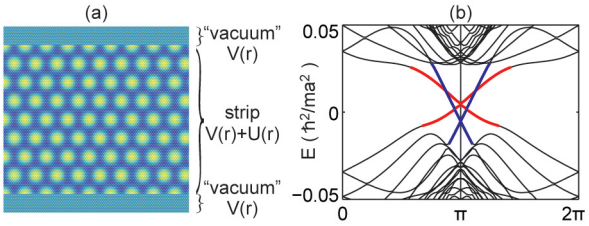

Fig. 4. (a) The strip model for calculation of edge states. (b) Band structure of the strip model. The gapless edge states are highlighted by red and blue lines.

conduction band of the host lattice. The distributions of $|F_{\bar{n}\boldsymbol{k}}|^2$ are mostly concentrated near the two valleys at K and K' of the host lattice Brillouin zone, which validates the assumptions of the effective-mass theory.

From Fig. 3 the components of the four impurity states at $\bar{K}$ can be readily seen, and it is found that $|A\uparrow\rangle > |B\downarrow\rangle > |B\uparrow\rangle > |A\downarrow\rangle$ by their energy. Then the order of the magnitudes of parameters in the Hamiltonian (10) can be determined, namely $-\xi < \Delta < \xi < \lambda$. This set of parameters indicates that the impurity superlattice lies in a topologically non-trivial regime. Calculations of the TB band structures can be found in SM [49]. The TB parameters lying in the topologically non-trivial regime reasonably reproduce the minibands, which indicates that the generalized Kane-Mele model (9) is indeed reliable for the description of the minibands.

The topological nature of the optical superlattice indicates the existence of topologically protected edge states, which we now confirm. We build a strip model in which the superlattice potential $U(\boldsymbol{r})$ is truncated to 4 period of the armchair direction and put on top of the host lattice potential $V(\boldsymbol{r})$, as shown in Fig. 4(a). Plane wave expansion is used to solve this strip model. The band structure near the energy window of the minibands is shown in Fig. 4(b). The gapless edge states as marked by red and blue lines can be readily seen. We have checked that the two pairs of states at $k = \pi$ are indeed lying at the two edges of the strip [49]. The existence of the gapless edge states provides a concrete evidence of the topological nature of the minibands, and validates the new effective-mass equation on which the generalized Kane-Mele model is built.

In the approach to creating SOC in an optical superlattice proposed above, an remarkable point is that the minibands only experience the influence of the host lattice via the effective mass, Berry curvature and quantum metric at the valleys. All high-energy degrees degrees of freedom are out of the picture. This is particularly advantageous, as it is clear from the new effective-mass equation (5) that the relative position, orientation and commensuration between the host and super lattices need not be precisely controlled to procure the geometric effects of the host lattice. Thus, the proposed approach is flexible. For example, Tarruell et al. [53] demonstrated experimentally that anisotropic massive Dirac cone dispersion can be created on an inversion symmetry-broken honeycomb lattice. Although anisotropic, this provides an equally ideal experimental host lattice for realizing the geometry-driven SOC and topological phase.

Putting the current effective-mass equation in a more general context, a richer variety of SOC effects can be achieved. For example, spins larger than 1/2 can be simulated on a host lattice with more than two valleys, and 3D SOC can be generated by a suitable constructed 3D host lattice. The effective SOC in this work does not flip spins. To generate an spin-flipping effective SOC, one may consider constructing a host lattice whose energy valley(s) consists of two or more degenerate bands acting as spins. Then the Berry curvature in the new effective-mass equation (5) is non-Abelian [45, 50], and its nonzero off-diagonal matrix elements can flip the spins.

In summary, the geometric effects of Bloch bands have highly non-trivial manifestation in the quantum states and spectrum, in the presence of a perturbation breaking discrete translational symmetry. In comparison with the traditional effective-mass equation, the geometric effects lead to two relativistic-like terms in the Hamiltonian, namely, the effective SOC and effective Darwin term. The new equation provides a novel perspective for understanding and tailoring wave mechanical states associated with imperfections of a host lattice, which can be any spatially periodic system including crystals, optical lattices, artificial superstructures, and so on. As an example, we demonstrate that the effective SOC can be exploited to induce non-trivial topology in an optical superlattice. This artificial SOC on cold atoms comes from the geometry of the band structure of the optical host lattice, and does not involve the internal structure of the atoms. Hence, this new scheme has a broad applicability on various kinds of atoms, and avoid the heating or

atom loss problem from spontaneous emission. The new effective-mass approximation can also be applied to other artificial superlattices, which is demonstrated in detail in the SM [49]. The formalism developed herein may also be profitably extended to photonic crystals, which are governed by the Maxwell equations.

ACKNOWLEDGMENTS

We are grateful to Di Xiao and Xibo Zhang for helpful discussions. This work is supported by Ministry of Science and Technology of the Peoples Republic of China (Grant Nos. 2018YFA0305601, 2016YFA0301004, 2017YFA0303302 and 2018YFA0305603), National Natural Science Foundation of China (Grant No. 11725415), and by Strategic Priority Research Program of Chinese Academy of Sciences, Grant No. XDB28000000. Q.N. is supported in the US by DOE (DE-FG03-02ER45958, Division of Materials Science and Engineering) on the general aspect of geometric phase effect, and by NSF (EFMA-1641101) and the Welch Foundation (F-1255).

[1] M. Z. Hasan and C. L. Kane, Rev. Mod. Phys. **82**, 3045 (2010).
[2] X.-L. Qi and S.-C. Zhang, Rev. Mod. Phys. **83**, 1057 (2011).
[3] J. Dalibard, F. Gerbier, G. Juzeliūnas, and P. Öhberg, Rev. Mod. Phys. **83**, 1523 (2011).
[4] H. Zhai, Int. J. Mod. Phys. B **26**, 1230001 (2012).
[5] V. Galitski and I. B. Spielman, Nature **494**, 49 (2013).
[6] N. Goldman, G. Juzelinas, P. hberg, and I. B. Spielman, Rep. Prog. Phys. **77**, 126401 (2014).
[7] H. Zhai, Rep. Prog. Phys. **78**, 026001 (2015).
[8] A. M. Dudarev, R. B. Diener, I. Carusotto, and Q. Niu, Phys. Rev. Lett. **92**, 153005 (2004).
[9] K. Osterloh, M. Baig, L. Santos, P. Zoller, and M. Lewenstein, Phys. Rev. Lett. **95**, 010403 (2005).
[10] J. Ruseckas, G. Juzeliūnas, P. Öhberg, and M. Fleischhauer, Phys. Rev. Lett. **95**, 010404 (2005).
[11] X.-J. Liu, M. F. Borunda, X. Liu, and J. Sinova, Phys. Rev. Lett. **102**, 046402 (2009).
[12] G. Juzeliūnas, J. Ruseckas, and J. Dalibard, Phys. Rev. A **81**, 053403 (2010).
[13] C. Zhang, Phys. Rev. A **82**, 021607 (2010).
[14] D. L. Campbell, G. Juzeliūnas, and I. B. Spielman, Phys. Rev. A **84**, 025602 (2011).
[15] B. M. Anderson, G. Juzeliūnas, V. M. Galitski, and I. B. Spielman, Phys. Rev. Lett. **108**, 235301 (2012).
[16] Z.-F. Xu, L. You, and M. Ueda, Phys. Rev. A **87**, 063634 (2013).
[17] B. M. Anderson, I. B. Spielman, and G. Juzeliūnas, Phys. Rev. Lett. **111**, 125301 (2013).
[18] X.-J. Liu, K. T. Law, and T. K. Ng, Phys. Rev. Lett. **112**, 086401 (2014).
[19] Y.-J. Lin, K. Jiménez-García, and I. B. Spielman, Nature **471**, 83 (2011).
[20] L. W. Cheuk, A. T. Sommer, Z. Hadzibabic, T. Yefsah, W. S. Bakr, and M. W. Zwierlein, Phys. Rev. Lett. **109**, 095302 (2012).
[21] P. Wang, Z.-Q. Yu, Z. Fu, J. Miao, L. Huang, S. Chai, H. Zhai, and J. Zhang, Phys. Rev. Lett. **109**, 095301 (2012).
[22] J.-Y. Zhang, S.-C. Ji, Z. Chen, L. Zhang, Z.-D. Du, B. Yan, G.-S. Pan, B. Zhao, Y.-J. Deng, H. Zhai, S. Chen, and J.-W. Pan, Phys. Rev. Lett. **109**, 115301 (2012).
[23] R. A. Williams, M. C. Beeler, L. J. LeBlanc, K. Jiménez-García, and I. B. Spielman, Phys. Rev. Lett. **111**, 095301 (2013).
[24] C. Qu, C. Hamner, M. Gong, C. Zhang, and P. Engels, Phys. Rev. A **88**, 021604 (2013).
[25] A. J. Olson, S.-J. Wang, R. J. Niffenegger, C.-H. Li, C. H. Greene, and Y. P. Chen, Phys. Rev. A **90**, 013616 (2014).
[26] L. Huang, Z. Meng, P. Wang, P. Peng, S. L. Zhang, L. Chen, D. Li, Q. Zhou, and J. Zhang, Nat. Phys. **12**, 540 (2016).
[27] Z. Wu, L. Zhang, W. Sun, X.-T. Xu, B.-Z. Wang, S.-C. Ji, Y. Deng, S. Chen, X.-J. Liu, and J.-W. Pan, Science **354**, 83 (2016).
[28] J. C. Slater, Phys. Rev. **76**, 1592 (1949).
[29] E. N. Adams, Phys. Rev. **85**, 41 (1952).
[30] C. Kittel and A. H. Mitchell, Phys. Rev. **96**, 1488 (1954).
[31] G. F. Koster and J. C. Slater, Phys. Rev. **95**, 1167 (1954).
[32] J. M. Luttinger and W. Kohn, Phys. Rev. **97**, 869 (1955).
[33] D. P. DiVincenzo and E. J. Mele, Phys. Rev. B **29**, 1685 (1984).
[34] S.-S. Li, J.-B. Xia, Z. L. Yuan, Z. Y. Xu, W. Ge, X. R. Wang, Y. Wang, J. Wang, and L. L. Chang, Phys. Rev. B **54**, 11575 (1996).
[35] G. Bastard, Phys. Rev. B **24**, 5693 (1981).
[36] G. Bastard, Phys. Rev. B **25**, 7584 (1982).
[37] M. G. Burt, J. Phys.: Condens. Matter **4**, 6651 (1992).
[38] H. Matsumura and T. Ando, J. Phys. Soc. Jpn. **67**, 3542 (1998).
[39] W. Kohn, Phys. Rev. **115**, 1460 (1959).
[40] G. H. Wannier, Phys. Rev. **117**, 432 (1960).
[41] J. J. Sakurai, *Advanced quantum mechanics* (Addison-Wesley, 1967).
[42] M. V. Berry, Proc. Roy. Soc. Lond. A **392**, 45 (1984).
[43] J. P. Provost and G. Vallee, Commun. Math. Phys. **76**, 289 (1980).
[44] M. V. Berry, in *Geometric phases in physics*, edited by F. Shapere and F. Wilczek (World Scientific, Singapore, 1989) pp. 7–28.
[45] D. Xiao, M.-C. Chang, and Q. Niu, Rev. Mod. Phys. **82**, 1959 (2010).
[46] J. Zhou, W.-Y. Shan, W. Yao, and D. Xiao, Phys. Rev. Lett. **115**, 166803 (2015).
[47] A. Srivastava and A. Imamoğlu, Phys. Rev. Lett. **115**, 166802 (2015).
[48] M. V. Berry, Proc. R. Soc. Lond. A **392**, 45 (1984).
[49] See Supplemental Material at [URL will be inserted by publisher] for details of the derivation of the new effective-mass equation, gauge transformation, band structure and Berry curvature distribution of the host lat-

tice, calculation of $\langle\psi_{n\boldsymbol{k}}|\Psi_{\bar{n}\bar{\boldsymbol{k}}}\rangle$, spatial distribution of edge states, tight-binding band structures, numerical simulations of muffin-tin potential, $\mathbb{Z}_2$ topological invariant, and remarks on the absence of geometric effects in traditional effective-mass equation..

[50] M.-C. Chang and Q. Niu, Journal of Physics: Condensed Matter **20**, 193202 (2008).

[51] G. Grynberg, B. Lounis, P. Verkerk, J.-Y. Courtois, and C. Salomon, Phys. Rev. Lett. **70**, 2249 (1993).

[52] C. L. Kane and E. J. Mele, Phys. Rev. Lett. **95**, 226801 (2005).

[53] L. Tarruell, D. Greif, T. Uehlinger, G. Jotzu, and T. Esslinger, Nature **483**, 302 (2012).